Electronic and Optical Modeling of Solar Cell Compounds $CuGaSe_2$ and $CuInSe_2$

Amit Soni, Alpa Dashora, Vikas Gupta, C. M. Arora, M. Rérat, B. L. Ahuja & Ravindra Pandey

Journal of Electronic Materials

ISSN 0361-5235
Volume 40
Number 11

Journal of Elec Materi (2011)
40:2197-2208
DOI 10.1007/s11664-011-1739-1

Springer

Journal of ELECTRONIC MATERIALS, Vol. 40, No. 11, 2011
DOI: 10.1007/s11664-011-1739-1

Electronic and Optical Modeling of Solar Cell Compounds $CuGaSe_2$ and $CuInSe_2$

AMIT SONI,[1] ALPA DASHORA,[2] VIKAS GUPTA,[3] C.M. ARORA,[3] M. RÉRAT,[4] B.L. AHUJA,[2,6] and RAVINDRA PANDEY[5]

1.—Department of Electrical Engineering, Global Institute of Technology (GIT), Jaipur 302 022, Rajasthan, India. 2.—Department of Physics, M.L. Sukhadia University, Udaipur 313 001, Rajasthan, India. 3.—Department of Electrical Engineering, Malaviya National Institute of Technology (MNIT), Jaipur 302 017, Rajasthan, India. 4.—Equipe de Chimie-Physique, IPREM UMR5254, Université de Pau et des Pays de l'Adour, av. du Président P. Angot, 64053 Pau Cedex, France. 5.—Department of Physics, Michigan Technological University, Houghton, MI 49931, USA. 6.—e-mail: blahuja@yahoo.com

We present dielectric-function-related optical properties such as absorption coefficient, refractive index, and reflectivity of the semiconducting chalcopyrites $CuGaSe_2$ and $CuInSe_2$. The optical properties were calculated in the framework of density functional theory (DFT) using linear combination of atomic orbitals (LCAO) and full-potential linearized augmented plane wave (FP-LAPW) methods. The calculated spectral dependence of complex dielectric functions is interpreted in terms of interband transitions within energy bands of both chalcopyrites; for example, the lowest energy peak in the $\varepsilon_2(\omega)$ spectra for $CuGaSe_2$ corresponds to interband transitions from Ga/Se-4p $\rightarrow$ Ga-4s while that for $CuInSe_2$ emerges as due to transition between Se-4p $\rightarrow$ In-5s bands. The calculated dielectric constant, $\varepsilon_1(0)$, for $CuInSe_2$ is higher than that of $CuGaSe_2$. The electronic structure of both compounds is reasonably interpreted by the LCAO (DFT) method. The optical properties computed using the FP-LAPW model (with scissor correction) are close to the spectroscopic ellipsometry data available in the literature.

Key words: Electronic structure, optical properties, absorption coefficients, solar cells

INTRODUCTION

Due to the many negative aspects of fossil-fuel energy sources, there is a great challenge to explore cheap, alternative sources of energy. In this context, photovoltaic (PV) generation is one of the most rapidly developing fields and is expected to serve as an alternative source of energy. The physics of semiconductor materials used in PV technology is governed by their energy bandgaps, optical properties, etc. When sunlight strikes the surface of a PV cell, its absorption depends on the energy bandgap of the semiconductor materials used in the construction of the solar cell. Among different materials, chalcopyrites such as $CuGaSe_2$ and $CuInSe_2$ may be promising semiconductor materials due to their applications in the areas of visible and infrared light-emitting diodes, solar cells, infrared detectors, optical parametric oscillators, upconverters, far-infrared generators, etc. These materials belong to the I–III–VI_2 family and are isoelectronic with zincblende semiconductors, with tetragonal space group D_{12}^{2d} with two formula units in each cell. Due to the technological applications of both materials, band-structure calculations and the optical properties of these materials have been reported using different quantum-mechanical models based on first-principles methods.

Jaffe and Zunger[1–3] used the all-electron mixed-basis potential-variation band-structure method within density functional theory (DFT) and also the potential-variation mixed-basis approach to study the electronic structure of some Cu-based ternary

(Received April 18, 2011; accepted August 16, 2011; published online September 20, 2011)

chalcopyrite semiconductors. The excitonic reflectivity spectra and the wavelength derivative reflection spectra for $CuGaSe_2$ were investigated by Syrbu et al.[4] Chalapathy and Reddy[5] reported chemical spray pyrolysis of $CuGaSe_2$ thin films and thereby studied its stoichiometry and crystallographic, morphological, optical, and electrical properties. Mudryi et al.[6] undertook photoluminescence studies on single crystals of $CuInSe_2$ and $CuGaSe_2$. Chichibu et al.[7] determined the bandgap and excitonic resonance energies of high-quality bulk single crystals of $CuInSe_2$ and $CuGaSe_2$ by means of photoreflectance, optical absorption, and photoluminescence measurements. Kawashima et al.[8] measured the complex dielectric functions and the absorption coefficient for the chalcopyrite semiconductors $CuGaSe_2$ and $CuInSe_2$ by using the spectroscopic ellipsometry (SE) technique at room temperature. Ahuja et al.[9] reported the optical properties of $CuGaS_2$ using the local density approximation (LDA) within the full-potential linear muffin-tin orbital (LMTO) method. Rodriguez et al.[10] used the Slater–Koster formalism to set a tight-binding Hamiltonian for Cu-based chalcopyrites including $CuInSe_2$. Alonso et al.[11] determined the optical functions and the electronic structure of $CuInSe_2$, $CuGaSe_2$, $CuInS_2$, and $CuGaS_2$ by the SE method. Using the LMTO method, Rashkeev and Lambrecht[12] calculated the energy bandgap of I-III-VI_2 chalcopyrite semiconductors including $CuGaSe_2$ and $CuInSe_2$. Belhadj et al.[13] used the all-electron full-potential linearized augmented plane wave (FP-LAPW) method within DFT with the LDA approach to investigate the structural, electronic, and optical properties of ternary chalcopyrite semiconductors. Jiang and Lambrecht[14] performed band-structure calculations of such materials using the LMTO method with an atomic sphere approximation. Electronic structure and total energy calculations for $Cu(Ga,In)Se_2$ using the first-principles full-potential LMTO method within the generalized gradient approximation (GGA) were performed by Medvedeva et al.[15] Chen et al.[16] reported the band structure of $CuGaSe_2$ using the plane-wave DFT GGA approach as implemented in the Vienna *ab initio* software package (VASP), and found that the GGA severely underestimates the bandgap. Reshak and Auluck[17] employed the FP-LAPW method to calculate the electronic structure, linear and nonlinear optical susceptibilities, and birefringence of $CuInX_2$ (X = S, Se, Te) chalcopyrites. Levchenko et al.[18] reported photoreflectivity, wavelength modulation spectroscopy, and photoluminescence measurements for determining the exciton band parameters and band structure of $CuGaSe_2$ at photon energies higher than the fundamental bandgap. Very recently, optical properties of $Cu(In,Ga)Se_2$ and $Cu_2ZnSn(S,Se)_4$ were reported by Zhao and Persson.[19]

Although there has been a sufficient drive to describe the electronic and optical properties of $CuGaSe_2$ and $CuInSe_2$, one of the curious features of the literature is the substantial disagreement between experimental and theoretical bandgaps. To rectify the electronic properties and to shed more light on the optical properties of such copper-based chalcopyrites, in this paper, we present for the first time the electronic and optical properties of $CuGaSe_2$ and $CuInSe_2$ using the linear combination of atomic orbitals (LCAO) method within DFT. Furthermore, to compare the applicability of the LCAO and FP-LAPW techniques, we have computed the electronic and optical properties using the FP-LAPW method. Another important concern of this work is to focus on the optical characteristics (and hence photovoltaic applications) of these materials using the interband transitions.

THEORETICAL METHODOLOGIES

Electronic band-structure calculations along with optical properties for both chalcopyrites $CuGaSe_2$ and $CuInSe_2$ were performed using the LCAO and the FP-LAPW methods. Outlines of the calculations are given below.

LCAO Method

LCAO is very useful for describing the ground-state electronic properties of materials. For the present computations, we used the CRYSTAL03 package,[20] which is based on the LCAO approach with DFT (LDA and GGA) and also *a posteriori* hybridization of Hartree–Fock (HF) and the DFT so-called Becke's three-parameter hybrid functional (B3LYP). It may be noted that, in the LCAO technique, the Bloch orbitals of the crystal are expanded using atom-centered Gaussian orbitals of s, p, or d symmetry.

In the DFT approach, it is assumed that the total ground-state energy of an electron system can be written as a functional of the electronic density $\rho(r)$. The Hamiltonian operator in this scheme is written as

$$\hat{h}_{\mathrm{KS}} = -\frac{1}{2}\nabla^2 + V_{\mathrm{ext}}(r) + \int \frac{\rho(\vec{r})}{|r-r'|}\mathrm{d}r' + \frac{\partial E_{\mathrm{XC}}[\rho(r)]}{\partial \rho(r)}, \tag{1}$$

where the first term represents the kinetic energy of the electron, the second term shows the external potential due to electron–nuclei interaction, and the third term corresponds to Coulombic repulsion. The last term deals with the exchange–correlation potential, where E_{XC} (the exchange–correlation density functional energy) is defined as

$$E_{\mathrm{XC}}[\rho(r)] = \int \rho(r)\varepsilon_{\mathrm{XC}}(r)\mathrm{d}r. \tag{2}$$

$\varepsilon_{\mathrm{XC}}$ is the exchange–correlation energy per particle in the electron gas. In the case of the LDA, it is assumed that the exchange–correlation energy at any point in space depends upon the $\rho(r)$ of a

homogeneous electron gas, while in the GGA, it depends not only on $\rho(r)$ but also on the gradient of $\rho(r)$.

In DFT-LDA, the calculations were performed by employing the Dirac–Slater exchange[20] and Perdew–Zunger (PZ) correlation potentials.[21] In the DFT-GGA scheme, we took the exchange and correlation functional of Perdew–Burke–Ernzerhof (PBE).[22] We also used the exchange potential given by Becke[23] and the correlation potential by Perdew–Wang (PW),[24] hereafter referred to as BPW. To see the effect of hybridization of HF and DFT, we chose the B3LYP approach, wherein E_{XC} is defined as

$$E_{XC} = (1-p)E_X^{LDA} + pE_X^{HF} + q\Delta E_X^{B88} + rE_C^{LYP} + (1-r)E_C^{VWN}. \quad (3)$$

The values (standard) of the prefactors p, q, and r were taken to be 0.20, 0.72, and 0.81, respectively. The value p = 0.20 leads to 20% mixing of the HF exchange with the LDA. ΔE_X^{B88} corresponds to Becke's gradient correction to the exchange functional. E_C^{LYP} and E_C^{VWN} are the correlation energies defined by Lee et al.[25] and Vosko et al.,[26] respectively.

The crystalline structure of the present chalcopyrites and the corresponding Brillouin zone (BZ) are shown in Fig. 1a, b. The lattice parameters for the tetragonal $CuGaSe_2$ were taken to be $a = b = 5.596$ Å and $c = 11.004$ Å, while the respective parameters for $CuInSe_2$ were 5.781 Å and 11.609 Å.[15] We used all-electron Gaussian basis sets for Cu, Ga, In, and Se from www.tcm.phy.cam.ac.uk/~mdt26/basis_sets. In the present computations, the Gaussian basis sets consisted of five s-, four p-, and two d-shells for Cu (86411/6411/41 set); five s-, four p-, and two d-shells for Ga (97631/7631/61 set); five s-, four p-, and two d-shells for Se (97631/7631/61 set); and six s-, five p-, and three d-shells for In (976311/76311/631). The basis sets, which also included the diffuse components, were energy-optimized using BILLY software.[20] The optimized outer-shell basis sets are given in Table I. The self-consistent calculations were performed at 288 $\boldsymbol{k}$ (15 15 15) points for both $CuGaSe_2$ and $CuInSe_2$ in the irreducible BZ (IBZ).

FP-LAPW Method

The FP-LAPW method as implemented in the Wien2k code[27] is among the most accurate methods for computing the electronic structure of materials. In this method, the unit cell is divided into interstitial region and nonoverlapping atomic spheres, known as muffin-tin (MT) spheres, which are centered at the atomic sites. Within the MT, the crystal potential is formed by spherical harmonics, while outside the MT it is represented by plane waves. The corresponding split representation of basis functions is defined using the relations

$$\varphi_{k+K_n}(r) = \frac{1}{\sqrt{\Omega}} e^{i(k+K_n)r} \quad r \in I(\text{interstitial region})$$

and

$$\varphi_{\mathbf{k}+\mathbf{K_n}}(S_\alpha + r) = \sum_{l}^{l_{max}} \left[C_{lm}^{\alpha}(k+K_n) u_l^{\alpha}(r, E_l) + D_{lm}^{\alpha}(k+K_n) \dot{u}_l^{\alpha}(r, E_l) \right] Y_{lm}(r) \quad |r| \le R_\alpha. \quad (4)$$

Here, S_α corresponds to the position vector of atomic nucleus α, while R_α is the radius of the MT sphere. $Y_{lm}(r)$ and $u_l^{\alpha}(r, E_l)$ are the spherical harmonics and the radial functions, respectively, whose product is the solution of the Schrödinger equation

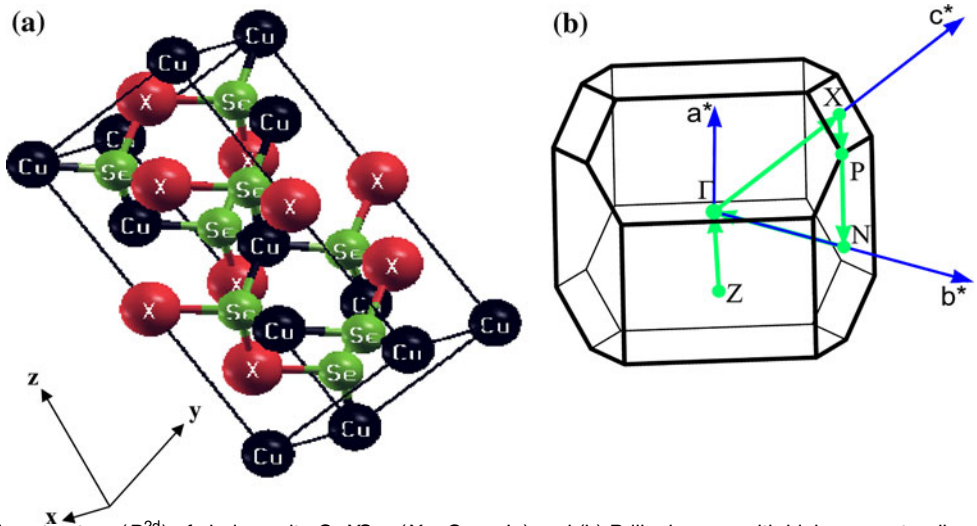

Fig. 1. (a) Crystalline structure (D_{12}^{2d}) of chalcopyrite $CuXSe_2$ (X = Ga or In) and (b) Brillouin zone with high-symmetry directions for the present D_{12}^{2d} structure. (Color figure online).

Table I. Optimized outer-shell basis sets for Cu, Ga, In, and Se in solid environment

Atom	Orbital	Exponent	Coefficient s	Coefficient p	Coefficient d
		$CuGaSe_2$			
Cu	sp	1.582	1.0	1.0	
	sp*	0.559	1.0	1.0	
	d	49.4656			0.0303
		13.6845			0.1603
		4.5962			0.378
		1.5122			0.4697
	d*	0.4251			1.0
Ga	d*	0.3841			1.0
	sp	3.9944	0.056	−0.0015	
		1.2875	0.285	0.0056854	
		0.2368	−0.2666	−0.171545	
	sp*	0.139608	1.0	1.0	
Se	d*	1.09082			1.0
	sp	2.318094	−0.908900	−0.1759	
		0.945900	−0.595800	0.5555	
		0.409815	3.163300	2.8121	
	sp*	0.1642	1.0	1.0	
		$CuInSe_2$			
Cu	sp	1.528	1.0	1.0	
	sp*	0.559	1.0	1.0	
	d	49.2489			0.0304
		13.7427			0.1601
		4.5958			0.3804
		1.5206			0.4677
	d*	0.4379			1.0
In	d*	0.2231			1.0
	sp	0.6254	1.0	1.0	
	sp*	0.1288	1.0	1.0	
Se	d*	1.0877			1.0
	sp	2.2557	−0.7084	−0.2044	
		0.8027	−0.1744	1.1752	
		0.3108	2.9708	4.3037	
	sp*	0.1066	1.0	1.0	

Gaussian exponents (in a.u.$^{-2}$) and contraction coefficients for sp and d states are collated. Asterisk indicates atomic orbitals assumed to be unoccupied at the beginning of the self-consistent field process.

for energy E_l. The second radial function $\dot{u}_l^z(r, E_l)$ is the derivative of $u_l^z(r, E_l)$ with respect to one electron energy. The coefficients C and D are computed for each atom in the unit cell with boundary conditions such as continuity of the basis function and the slope of the MT surfaces.

The solutions to the Kohn–Sham equations are expanded as

$$\psi_{\mathbf{k}+\mathbf{K_n}}(r) = \sum_{\mathbf{k}+\mathbf{K_n}}^{K_{\max}} c_{\mathbf{k}+\mathbf{K_n}} \varphi_{\mathbf{k}+\mathbf{K_n}}(r), \tag{5}$$

where the coefficients $c_{\mathbf{k}+\mathbf{K_n}}$ are determined by the Rayleigh–Ritz variational principle. The convergence of this basis set is controlled by a cutoff parameter $R_{\mathrm{MT}}K_{\max}$, where R_{MT} is the smallest atomic sphere radius in the unit cell and $\boldsymbol{K}_{\max}$ is the magnitude of the largest $\boldsymbol{K}$ vector.

Therefore, the FP-LAPW allows a better description of the rapidly changing wavefunctions, potentials, and electron density close to the nuclei, and also the smoother part of these quantities in between the atoms.

To account for exchange and correlation effects, we used the gradient-corrected functionals reported by PBE.[22] In addition, we also employed the latest GGA potentials prescribed by Wu and Cohen (WC).[28] R_{MT} in $CuInSe_2$ was 2.42 a.u., 2.69 a.u., and 2.18 a.u. for Cu, In, and Se, respectively. The values of R_{MT} in $CuGaSe_2$ were 2.40 a.u., 2.49 a.u., and 2.10 a.u., respectively for Cu, Ga, and Se. For both compounds, the calculations were performed with 158 $\boldsymbol{k}$ points. The values of other governing parameters[27] such as the cutoff for charge density ($G_{\max}$), maximum radial expansion ($l_{\max}$), and $R_{\mathrm{MT}}K_{\max}$ were set as 14, 10, and 8, respectively.

Optical Properties

An important aspect of optical properties can be discussed by means of the transverse dielectric function, which depends on the momentum transfer $\mathbf{q}$ in the photon–electron interaction and the energy transfer ω.

At lower energy (like that of solar radiation), one can assume $\mathbf{q} = 0$ and consider only the electric-dipole approximation. The total dielectric function is $\varepsilon(\omega) = \varepsilon_1(\omega) + i\varepsilon_2(\omega)$, where ε_1 is the frequency-dependent real part while ε_2 corresponds to the imaginary part.

Direct interband transitions, which are important for semiconducting materials, contribute to the imaginary part $\varepsilon_2(\omega)$. Considering the appropriate transition matrix elements, $\varepsilon_2(\omega)$ is calculated by summing all possible transitions from the occupied to unoccupied states.

Within the notations of the FP-LAPW,[27,29] $\varepsilon_2(\omega)$ is given by

$$\varepsilon_2^{\mathrm{IBZ}}(\omega) = \frac{8\pi^2 e^2 \hbar}{m^2\omega^2} \sum_{\mathrm{v,c}} \int |M_{\mathrm{cv}}(k)|^2 \delta\{\omega_{\mathrm{cv}}(k) - \omega\} \frac{d^3k}{(2\pi)^3}. \tag{6}$$

The integration in Eq. (6) is initially calculated only in the IBZ. The total $\varepsilon_2(\omega)$ is obtained after considering the symmetry operations.

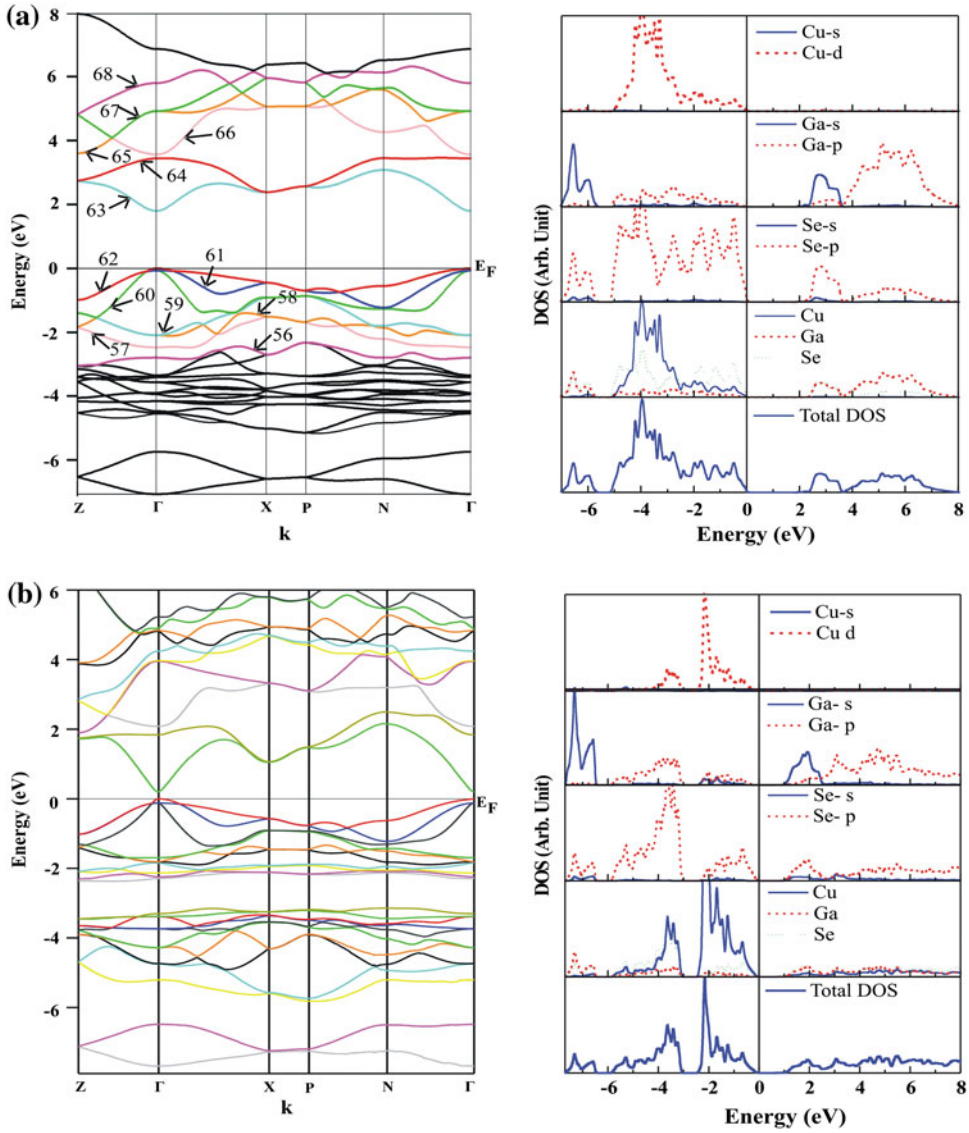

Fig. 2. Band structure and density of states (DOS) of $CuGaSe_2$ using (a) LCAO-DFT-GGA and (b) FP-LAPW schemes. The bands are shown in different directions framed by the vertices Z (0.5 0.5 −0.5), Γ (0 0 0), X (0 0 0.5), P (0.25 0.25 0.25), and N (0 0.5 0). Numbering of energy bands based on the convention of the Wien2k (FP-LAPW) code, marked from the lowest energy side (viz. the lowest energy band at −69.22 eV is band number 1). (Color figure online).

M_{cv} in Eq. (6) is defined as

$$M_{cv}(k) = \langle u_{ck}|e \cdot \nabla|u_{vk}\rangle. \tag{7}$$

Here, e corresponds to the potential vector and represents the electric field. $u_{vk}(r)$ and $u_{ck}(r)$ represent the valence-band and conduction-band states in which the direct transitions are possible. The transition energy $\hbar\omega_{cv}$ is equal to $E_{ck} - E_{vk}$.

After calculating $\varepsilon_2(\omega)$, the real part $\varepsilon_1(\omega)$ can be derived using the Kramers–Kronig relations. Mathematically,

$$\varepsilon_1(\omega) = 1 + \frac{2}{\pi}\wp\int_0^\infty \frac{\omega'\varepsilon_2(\omega')}{\omega'^2 - \omega^2}d\omega', \tag{8}$$

where $\wp$ indicates the principal value of the integral.

In the case of LCAO computations, the sum-over-states methodology[30] is used to derive the real and imaginary parts of the dynamic polarizability $P(\omega)$ as a function of ω. $P(\omega)$ can be expressed as

$$P(\omega) = \sum_{\mathbf{p}} \Omega_{\mathbf{p}} \sum_{mn} f_{mn\mathbf{p}} \left[\frac{\Delta\varepsilon^2_{mn\mathbf{p}} - \omega^2 + i\eta\omega}{\left(\Delta\varepsilon^2_{mn\mathbf{p}} - \omega^2\right)^2 + \eta^2\omega^2}\right], \tag{9}$$

where $f_{mn\mathbf{p}}$ are oscillator strengths using the velocity operator between valence and conduction crystalline orbitals for each point $\mathbf{p}$ with geometric weight $\Omega_{\mathbf{p}}$. $\Delta\varepsilon_{mn\mathbf{p}}(= \varepsilon_{n\mathbf{p}} - \varepsilon_{m\mathbf{p}})$ are the corresponding vertical transition energies, and η is the damping factor corresponding to the inverse lifetime (average value) of the excited states. Then, the real and imaginary parts $\varepsilon_1(\omega)$ and $\varepsilon_2(\omega)$ can be calculated.

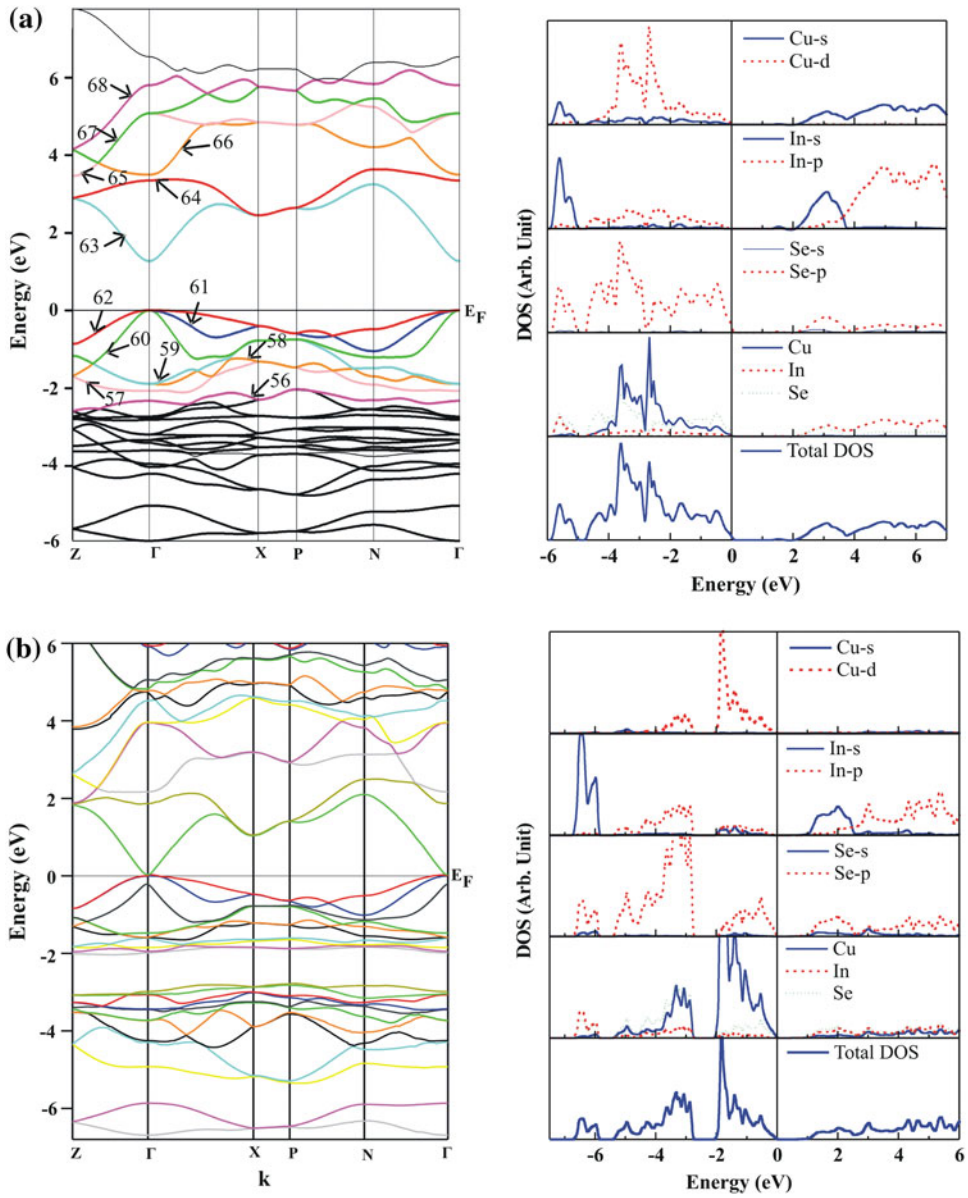

Fig. 3. Band structure and density of states (DOS) of $CuInSe_2$ using (a) LCAO-DFT-GGA and (b) FP-LAPW approaches. Numbering of energy bands based on the convention of the Wien2k (FP-LAPW) code. (Color figure online).

In the present computations, the value of η was taken as 0.25 eV.

It is known that the absorption coefficient is basically a measure of how far light with a specific energy can penetrate the material before absorption. The absorption coefficient $\alpha(\omega)$ can be calculated from the dielectric components $\varepsilon_1(\omega)$ and $\varepsilon_2(\omega)$ using the following expression:

$$\alpha(\omega) = \sqrt{2}\omega\left[\left\{\varepsilon_1^2(\omega) + \varepsilon_2^2(\omega)\right\}^{1/2} - \varepsilon_1(\omega)\right]^{1/2}. \quad (10)$$

Alternatively, one can also reformulate the absorption coefficients using extinction coefficients.[29]

The normal incidence of reflectivity can be obtained by using the following relation:

$$R = \frac{[n(\omega)-1]^2 + k(\omega)^2}{[n(\omega)+1]^2 + k(\omega)^2}, \quad (11)$$

where $n(\omega)$ and $k(\omega)$ are the real and imaginary parts of the complex refractive index. Mathematically, $n(\omega)$ and $k(\omega)$ are defined as

$$n(\omega) = \sqrt{\frac{|\varepsilon(\omega)| + \varepsilon_1(\omega)}{2}}, \quad (12)$$

and

$$k(\omega) = \sqrt{\frac{|\varepsilon(\omega)| - \varepsilon_1(\omega)}{2}},$$
$$\text{with } |\varepsilon(\omega)| = \sqrt{\varepsilon_1(\omega)^2 + \varepsilon_2(\omega)^2}. \quad (13)$$

RESULTS AND DISCUSSION

Energy Bands and Density of States

Figures 2a, b and 3a, b show the energy bands (left panel) along high-symmetry directions of the BZ and density of states (DOS) (right panel) for $CuGaSe_2$ and $CuInSe_2$ by using the LCAO-GGA (PBE) and FP-LAPW (PBE) methodologies. Both figures show that the present chalcopyrites are direct-bandgap semiconductors at the Γ point. The topology of the energy bands and the DOS computed using the LCAO-LDA and LCAO-B3LYP methods are found to be similar to the LCAO-GGA (PBE) except for some fine structures and the magnitude of the bandgap. Moreover, the shape of the energy bands found using the LCAO-GGA (PBE) and LCAO-GGA (BPW) methods were found to be the same, with negligible difference (0.01 eV) in bandgap. Therefore, we do not show the energy bands and DOS obtained at the level of the LCAO-LDA, LCAO-B3LYP, and LCAO-GGA (BPW) approximations.

The energy bands of $CuGaSe_2$ (Fig. 2a) in the energy range of 1.8 eV to 8.0 eV exist due to the hybridization of Ga (4sp) and Se (4sp). On the other hand, the valence bands in the energy range from −5.2 eV to 0.0 eV are associated with the Cu (3d), Ga (4p), and Se (4p) states. A minor presence of Ga (4s) and Se (4s) can be noticed in this region. The lowermost valence bands in the region from −5.5 eV to −7.0 eV mainly originate due to the hybridization of Ga (4s) and Se (4p) states along with a small contribution from Ga (4p) and Se (4s) states.

The FP-LAPW (PBE)-based energy bands of $CuGaSe_2$ (Fig. 2b) were found to be almost identical (except the bandgap and slight shifting of energy bands) to those deduced from FP-LAPW (WC). The FP-LAPW (PBE)-based topmost group of energy bands of $CuGaSe_2$ (conduction region) in the energy range from 0.2 eV to 6.0 eV are mainly due to the hybridization of Ga (4sp) and Se (4sp) states. In the valence-band region, a group of bands in the energy range from 0.0 eV to −2.6 eV are ascribed to the hybridization of Cu (3d) and Se (4p) states. The bands within the range from −3.0 eV to −5.9 eV originate from the Cu (3d), Ga (4p), and Se (4p) states, while the lowest energy bands are formed by the Ga (4sp) and Se (4sp) states.

Now we discuss the difference between the energy bands of $CuGaSe_2$ (Fig. 2a, b) derived by the LCAO-GGA (PBE) and FP-LAPW (PBE) methods. Although the overall shape of the energy bands deduced from both the LCAO-GGA (PBE) and FP-LAPW (PBE) schemes seems to be almost identical, there are significant differences in the position of energy bands in the valence region. In the upper valence region, the energy bands with labeling 62 to 57 (0.0 eV to −2.62 eV) in the LCAO-GGA (PBE) scheme are found to be less dispersed (between 0.0 eV to −1.94 eV) in the FP-LAPW (PBE) calculations. The next group of four bands, corresponding to Cu (3d), Ga (4p), and Se (4p) states, lie within the energy ranges from −2.33 eV to −3.47 eV and from −1.87 eV to −2.40 eV in case of the LCAO-GGA (PBE) and FP-LAPW (PBE) schemes, respectively. A systematic shift and larger dispersion of energy

Table II. Calculated direct bandgap at Γ (in eV) for $CuGaSe_2$ and $CuInSe_2$, along with available theoretical and experimental data

	Bandgap (eV)	
Method	**$CuGaSe_2$**	**$CuInSe_2$**
Present work		
(a) LCAO		
LDA (PZ)	1.62	1.05
GGA (PW)	1.78	1.25
GGA (PBE)	1.79	1.26
B3LYP	3.12	2.59
(b) FP-LAPW		
GGA (WC)	0.093	0.035
GGA (PBE)	0.199	0.035
Previous results		
(a) FP-LAPW		
LDA (PW)	0.83[a]	0.26[a]
LDA	–	0.41[b]
(b) PVMB		
LDA (CA)	0.48[c]	–0.2[c]
(c) Slater–Koster formalism	–	–1.55[d]
(d) Plane-wave code (VASP)		
GGA (PW91)	0.03[e]	–
(e) PAPW		
GGA (PBE)	0.21[f]	0.0[f]
HSE	1.35[f]	0.76[f]
GW	1.56[f]	0.79[f]
(f) LMTO		
LDA	0.20[g]	0.01[g]
(g) FP-LMTO		
GGA (PBE)	0.28[h]	0.0[h]
Available experiment		
(a) Photoluminescence measurements	1.73[i]	1.04[i]
(b) Chemical spray pyrolysis	1.69[j]	–
(c) MOVPE method	–	1.03[k]

In column 1, the correlation potentials used by different workers are also given in parenthesis; *PVMB* potential variation mixed basis, *PZ* Perdew and Zunger, *LMTO*, linear muffin-tin orbital, *PW* Perdew and Wang, *VASP* Vienna *ab initio* software package, *PBE* Perdew, Becke, and Ernzerhof, *FP-LMTO* full-potential linear muffin-tin orbital, *CA* Ceperley and Adler, *MOVPE* metalorganic vapor-phase epitaxy, *GW* Green's function approach, *HSE* Heyd, Scuseria, and Ernzerhof, *PAPW*, projector augmented plane wave; [a]Belhadj et al.[13]; [b]Reshak and Auluck[17]; [c]Jaffe and Zunger[2]; [d]Rodriguez et al.[10]; [e]Chen et al.[16]; [f]Zhao and Persson[19]; [g]Rashkeev and Lambrecht[12]; [h]Medvedeva et al.[15]; [i]Mudryi et al.[6]; [j]Chalapathy and Reddy[5]; [k]Chichibu et al.[7]

bands in the LCAO-GGA (PBE) calculations as compared with the FP-LAPW method are also visible in the corresponding DOS curves (Fig. 2a, b).

Now we discuss the 11 FP-LAPW (PBE)-based energy bands which are found in the energy range from −3.14 eV to −5.84 eV (Fig. 2b). It is observed that these bands appear in the energy range from −5.16 eV to −3.27 eV in case of LCAO-GGA (PBE) (Fig. 2a), resulting in a broad shape of the DOS structure in the energy range from 0.0 eV to −5.16 eV.

For the conduction region, the total number of bands is different in the LCAO-GGA (PBE) and the FP-LAPW (PBE) schemes, which is attributed to an incomplete nature of the diffuse basis sets in the LCAO-GGA (PBE) scheme.

The energy bands and DOS of $CuInSe_2$ are shown in Fig. 3a, b. Except for different values of energy ranges in the LCAO-GGA (PBE) and the FP-LAPW (PBE), it is mainly observed that the conduction bands are formed due to the hybridization of In (5sp) and Se (4sp) states. The valence bands below the Fermi energy (E_F) arise from Cu (3d) and Se (4p) states. Slight hybridization of In (5sp) and Se (4s) states is also found in these bands. Furthermore, Se (4s) state negligibly contributes in the lowermost region of valence bands. As for $CuGaSe_2$, the DOS curves for $CuInSe_2$ (Fig. 3a, b) computed using the LCAO-GGA (PBE) and FP-LAPW (PBE) schemes also differ in the valence region. This may also be explained by the position of the energy bands.

The bandgaps, for $CuGaSe_2$ and $CuInSe_2$, derived from the different schemes of the LCAO and FP-LAPW methods along with available data, are collated in Table II. Among the LCAO approximations, the bandgaps calculated using DFT (LDA and GGA with both the BPW and PBE) are found to be close to the experimental data. GW (where G means Green function and W stands for screened Coulomb interaction) calculations[19] also show close agreement with the experimental data.[6] The bandgaps computed using the FP-LAPW (WC) method are found to be very small (0.093 eV for $CuGaSe_2$ and 0.035 eV for $CuInSe_2$). The FP-LAPW (PBE) calculations for $CuGaSe_2$ show almost twice the bandgap value in comparison with FP-LAPW (WC). Although the smaller bandgap values obtained using the present FP-LAPW calculations (even with the latest GGA prescription) are close to LMTO and plane-wave calculations,[12,15] these values cannot be reconciled with experimental data. As seen also in our earlier work,[31,32] the significant difference between the bandgaps obtained from the present FP-LAPW and LCAO calculations is mainly due to the different nature of the basis sets, as discussed earlier (Gaussian in LCAO, and MT-based full potentials in LAPW).

It is worthwhile to mention that the smaller bandgaps computed using the FP-LAPW model and also predicted by various authors[1,5–7,10,12,13,15–17] as given in Table II seem to be unreliable in such type of semiconducting materials. It may be noted that

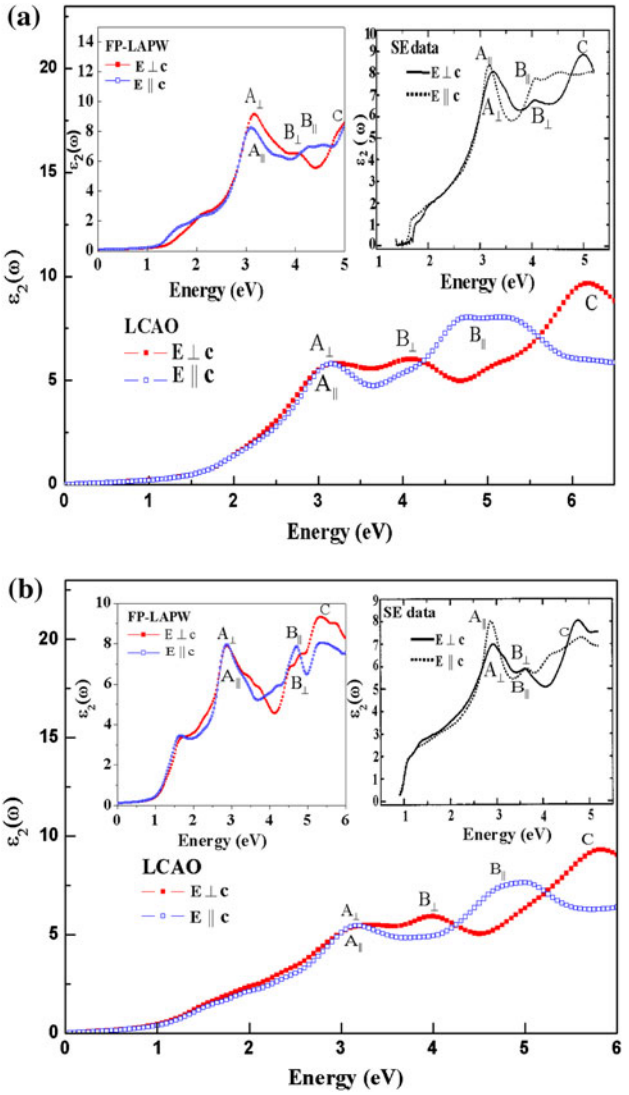

Fig. 4. Imaginary part of the dielectric tensor (ε_2) using the LCAO method for $E \perp c$ and $E \parallel c$ for (a) $CuGaSe_2$ and (b) $CuInSe_2$. Spectroscopic ellipsometry (SE) data reported by Alonso et al.[11] and present FP-LAPW (with scissor correction) data are also shown inset. (Color figure online).

the optical properties of semiconductors may be affected by the attractive interaction between photoexcited electrons (in the conduction bands) and the holes that they leave behind in the valence bands. To include the electron–hole interaction (excitonic) effects, one can also consider a two-particle formalism, solving the Bethe–Salpeter equation (BSE). Since Wien2k and CRYSTAL03 do not incorporate the BSE formalism, we could not check excitonic contribution in the present work.

Dielectric Properties

The imaginary parts of the frequency-dependent dielectric functions $\varepsilon_2(\omega)$ for $CuGaSe_2$ and $CuInSe_2$ computed using the LCAO-GGA (PBE) method are shown in Fig. 4a, b. For both chalcopyrites, we also show (inset) the SE data reported by Alonso et al.[11]

Table III. Comparison of peak positions in $\varepsilon_2(\omega)$ data of $CuGaSe_2$ and $CuInSe_2$ computed using the LCAO and FP-LAPW (with scissor correction) schemes (from Fig. 4a, b)

		Peaks (eV)				
$\varepsilon_2(\omega)$	Method	$A_\perp$	$A_\parallel$	$B_\perp$	$B_\parallel$	C
$CuGaSe_2$	LCAO-GGA (PBE)	3.2	3.2	4.2	4.7	6.2
	FP-LAPW (PBE)	3.2	3.1	4.0	4.4	5.0
	SE data[a]	3.3	3.2	4.0	4.1	5.0
$CuInSe_2$	LCAO	3.2	3.2	4.0	4.8	5.8
	FP-LAPW	2.9	2.9	4.5	4.7	5.4
	SE data[a]	2.9	2.8	3.6	3.6	4.8

Experimental spectroscopic ellipsometry (SE) data are also incorporated in this table; [a]Alonso et al.[11]

Table IV. Optical dielectric constant (ε_1) and refractive index (n) for $CuGaSe_2$ and $CuInSe_2$ along with available data

	$\varepsilon_1(0)$	$\varepsilon_1^\perp(0)$	$\varepsilon_1^\parallel(0)$	$n(0)$	$n_\perp(0)$	$n_\parallel(0)$
$CuGaSe_2$						
(i) Present work						
LCAO-GGA	4.60	4.65	4.49	2.14	2.16	2.12
FP-LAPW-GGA	8.46[a]	8.49[a]	8.40[a]	2.90[a]	2.91[a]	2.89[a]
	12.73[b]	12.80[b]	12.60[b]	3.59[b]	3.48[b]	3.82[b]
(ii) Previous results						
FP-LAPW-LDA[c]	8.15			4.04		
PAPW-HSE[d]		7.31	7.25			
PAPW-GW[d]		8.51	8.42			
$CuInSe_2$						
(i) Present work						
LCAO-GGA	4.87	4.94	4.73	2.21	2.22	2.17
FP-LAPW-GGA	8.51[a]	8.53[a]	8.48[a]	2.92[a]	2.92[a]	2.91[a]
	12.80[b]	12.78[b]	12.84[b]	3.58[b]	3.57[b]	3.58[b]
(ii) Previous results						
FP-LAPW-LDA[c]	7.64			3.91		
PAPW-HSE[d]		8.18	7.62			
PAPW-GW[d]		8.26	7.83			
FP-LAPW-LDA[e]	14.73	14.8	14.6	2.83		

Symbols $\perp$ and $\parallel$ correspond to polarization along the x and y-directions, and towards the z-direction, respectively, as given in the text; [a]With scissor correction; [b]Without scissor correction; [c]Belhadj et al.[13]; [d]Zhao and Persson[19]; [e]Reshak and Auluck.[17]

and the present FP-LAPW (PBE) calculations. In the present D_{12}^{2d} structure, $\varepsilon_2(\omega)$ is resolved into two components, namely (a) $\varepsilon_2^\perp(\omega)$, which is the average of the spectra for polarization along the x and y-directions ($E \perp c$), and (b) $\varepsilon_2^\parallel(\omega)$, corresponding to the polarization towards the z-direction ($E \parallel c$). To show the anisotropies in the optical properties, we calculated both components $\varepsilon_2^\parallel(\omega)$ and $\varepsilon_2^\perp(\omega)$.

The $\varepsilon_2(\omega)$ spectra for $CuGaSe_2$ derived from the LCAO-GGA (PBE) calculations are shown in Fig. 4a. Different peaks in this figure can be explained with the help of interband transitions from the valence to conduction bands, as marked in Fig. 2a. The features in $\varepsilon_2(\omega)$ are mostly governed by the joint density of states. The structure in the joint density of states is associated with the region in the band structure where bands are almost parallel. The peaks $A_\perp$ and $A_\parallel$ observed at the energy level 3.2 eV originate from interband transitions from the 62nd to 64th band (in ZΓ, ΓX, and NΓ directions, where bands are nearly parallel). These transitions mainly correspond to Se (4p) to Ga (4s) states, as can be seen from the DOS curves shown in Fig. 2a. The peak $B_\perp$ (at 4.2 eV) corresponds to transitions taking place from the 59th to 63rd band (along ZΓ and ΓX branches). Mostly, transitions from the 60th to 67th band (in ZΓ direction) lead to peak $B_\parallel$ at 4.7 eV. Peak C at 6.2 eV can be explained with the help of transitions from bands $57 \rightarrow 65$ and $58 \rightarrow 66$ in XP direction.

In case of LCAO-GGA (PBE) calculations for $CuInSe_2$ (Fig. 4b), peaks $A_\perp$ and $A_\parallel$ (at 3.2 eV)

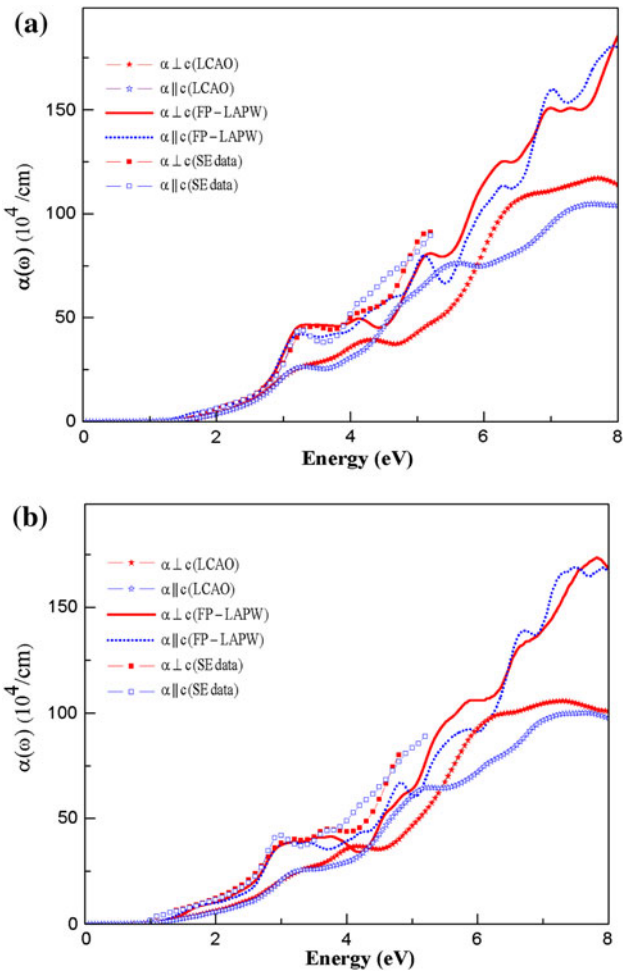

Fig. 5. Absorption coefficient (α) for (a) $CuGaSe_2$ and (b) $CuInSe_2$ computed using LCAO-GGA and FP-LAPW (with scissor correction) methods along with spectroscopic ellipsometry (SE) data reported by Alonso et al.[11] Perpendicular and parallel components correspond, respectively, to polarization along the *x* and *y*-directions ($E \perp c$), and towards the *z*-direction ($E \parallel c$). (Color figure online).

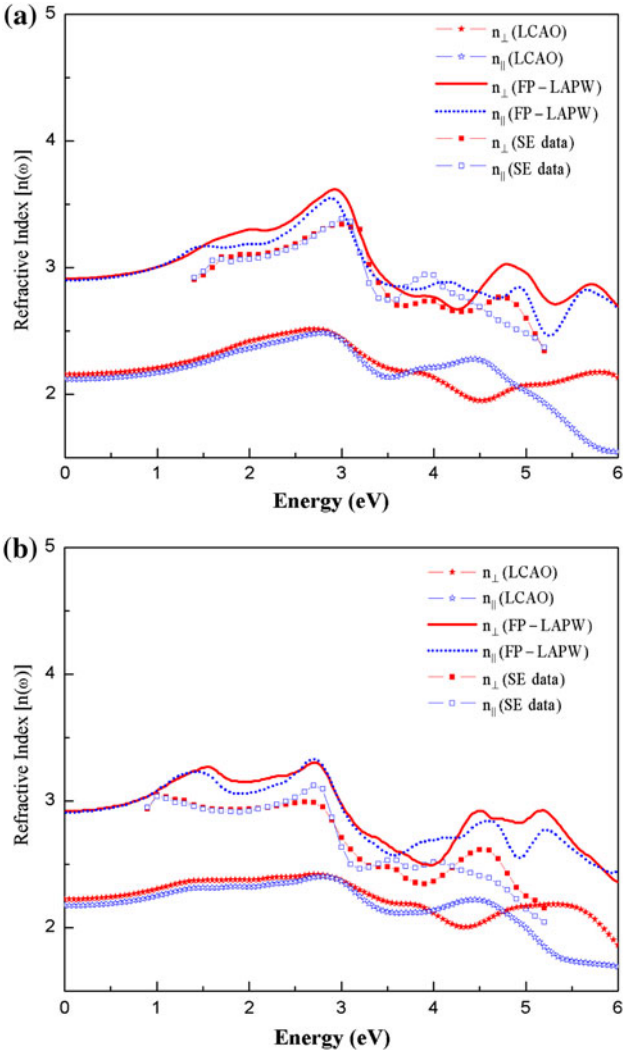

Fig. 6. Real part of the refractive index $n(\omega)$ for (a) $CuGaSe_2$ and (b) $CuInSe_2$ computed using the LCAO-GGA and FP-LAPW (with scissor correction) methods along with spectroscopic ellipsometry (SE) data reported by Alonso et al.[11] Perpendicular and parallel components correspond, respectively, to polarization along the *x* and *y*-directions ($E \perp c$), and towards the *z*-direction ($E \parallel c$). (Color figure online).

emerge due to transition between the 62nd and 64th bands (Fig. 3a), corresponding to Se (4p) $\rightarrow$ In (5s) states. Peak $B_\perp$ (at 4.0 eV) is a result of transition from the 59th to 63rd band along ZΓ and ΓX directions, while the parallel component $B_\parallel$ (at 4.8 eV) involves transitions from the 57th to 63rd band and may also be due to transition from the 56th to 64th bands (in XP direction). Peak C (at 5.8 eV) can be explained by transitions from the 57th to 65th and 58th to 66th bands in XP direction.

Since FP-LAPW calculations underestimated the bandgap for both chalcopyrites, for the computation of optical spectra, we adopted the scissor correction (to adjust the DFT bandgap to the experimental value) as facilitated in the Wien2k code.[26] As for LCAO calculations, the origin of different peaks in the FP-LAPW-based $\varepsilon_2(\omega)$ spectra, as shown inset to Fig. 4a, b, can be understood in terms of the energy bands as shown in Figs. 2b and 3b. A comparison of peak positions in the experimental and theoretical $\varepsilon_2(\omega)$ spectra is summarized in Table III. Considering the amplitude and position of the different peaks in the $\varepsilon_2(\omega)$ spectra, it is observed that the present FP-LAPW (PBE) calculations with an *ad hoc* scissor correction show close agreement with the available SE data.[11] Separately, in the LCAO calculations it is observed that $\varepsilon_2(\omega)$ decreases after 7 eV and becomes almost negligible just below 14 eV, while the conduction bands are formed up to a maximum energy of 20 eV. This trend is also in tune with our FP-LAPW calculations.

Values of dielectric constant, $\varepsilon_1(0)$, derived from the LCAO-GGA (PBE) and the FP-LAPW (PBE) calculations along with available theoretical data are given in Table IV. It is seen that $\varepsilon_1(0)$ for $CuInSe_2$ is higher than that of $CuGaSe_2$, which

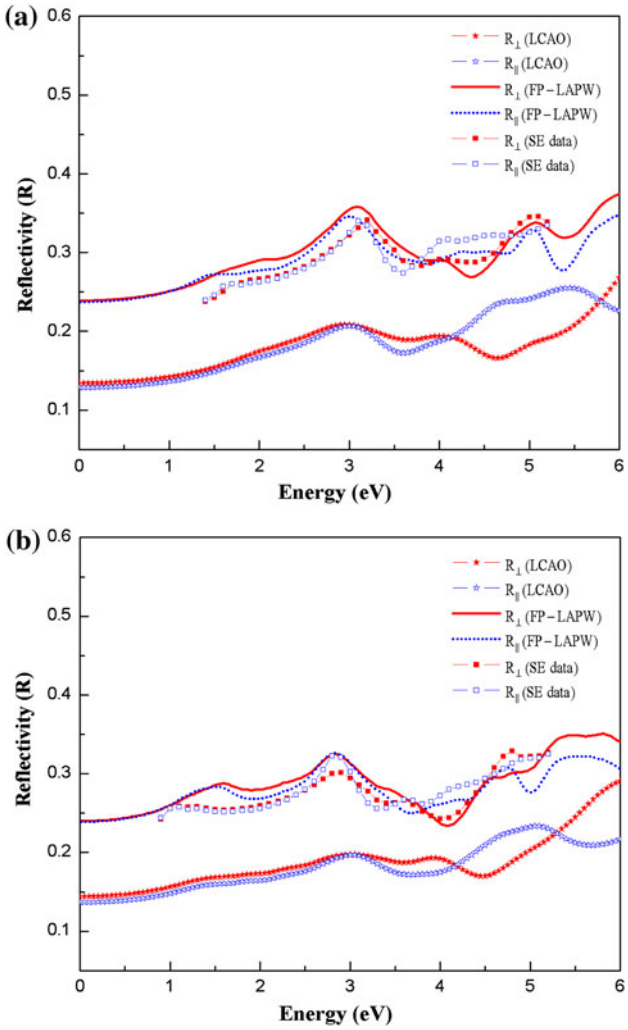

Fig. 7. Reflectivity spectra for (a) $CuGaSe_2$ and (b) $CuInSe_2$ computed using LCAO-GGA and FP-LAPW (with scissor correction) methods along with spectroscopic ellipsometry (SE) data reported by Alonso et al.[11] Perpendicular and parallel components correspond, respectively, to polarization along the *x* and *y*-directions ($E \perp c$), and towards the *z*-direction ($E \parallel c$). (Color figure online).

could be explained on the basis of the Penn model,[33] where $\varepsilon_1(0)$ is related to the energy bandgap (ΔE_g) by the approximation $\varepsilon_1(0) \approx 1 + (\hbar\omega_P/\Delta E_g)^2$. Here, ω_P is the valence electron plasmon frequency. The higher value of $\varepsilon_1(0)$ obtained from the FP-LAPW method can also be explained on the basis of the low value of ΔE_g predicted by the FP-LAPW method.

Absorption Coefficient, Refractive Index, and Optical Reflectivity

The perpendicular and parallel components of the absorption coefficient (α) for $CuGaSe_2$ and $CuInSe_2$ computed using the LCAO-GGA (PBE) and the FP-LAPW (PBE with scissor correction) schemes along with the available experimental data[11] are plotted in Fig. 5a and b, respectively. It is seen that, in the low energy range, the position of different peaks or peculiar structures in both theories are consistent with the experimental data of Alonso et al.[11] The values of the energy-dependent absorption coefficients derived from the LCAO-GGA (PBE) calculation are found to be smaller than the FP-LAPW (PBE with scissor correction) data.

Figure 6a, b shows plots of the real part of the refractive index $n(\omega)$ for $CuGaSe_2$ and $CuInSe_2$ using the LCAO-GGA (PBE) and FP-LAPW (PBE) methods. The value of birefringence (the difference between the extraordinary and ordinary refraction indices, $\Delta n(\omega) = n_\perp(\omega) - n_\parallel(\omega)$, where $n_\parallel(\omega)$ is the index of refraction for an electric field oriented along the *c*-axis and $n_\perp(\omega)$ is the index of refraction for an electric field perpendicular to the *c*-axis) in the low energy range as computed using FP-LAPW (PBE) and the SE data is smaller than that at higher energy. Although not in amplitude, the position of the different peaks in the low energy range computed using LCAO-GGA (PBE) is in agreement with the FP-LAPW (PBE) and SE data. Table IV shows that the incorporation of the scissor correction in the FP-LAPW (PBE) scheme reduces the value of refractive index significantly.

The optical reflectivity for both compounds calculated using the LCAO-GGA (PBE) and FP-LAPW (PBE) methods is shown in Fig. 7a, b, together with the SE data of Alonso et al.[11] In both cases, the amplitude of LCAO-based reflectivity starts at about 0.15, whereas the FP-LAPW-based reflectivity is more than twice this value. A peak-like structure in the experimental reflectivity data[11] at about 3 eV is also visible in the LCAO-GGA (PBE) and FP-LAPW (PBE) calculations. Other structures seen in the SE data are also consistent with the LCAO-GGA (PBE) and FP-LAPW (PBE) computations.

It is worth mentioning that the energy spectrum of solar radiations lies between 0 eV and 5 eV. Reasonable values of the absorption coefficient and peaks in $\varepsilon_2(\omega)$ spectra in the energy range from 3 eV to 5 eV depict the usefulness of both investigated chalcopyrites in solar cells.

CONCLUSIONS

In this paper, electronic and optical properties of solar cell materials $CuGaSe_2$ and $CuInSe_2$ were calculated using different prescriptions of exchange and correlation in the LCAO-DFT and FP-LAPW techniques. It is concluded that the bandgaps in $CuGaSe_2$ and $CuInSe_2$ computed using the LCAO-DFT (LDA/GGA) technique are close to the experimental data. The FP-LAPW model with exchange and correlation potentials prescribed by Perdew–Burke–Ernzerhof and also Wu and Cohen underestimates the bandgap value in $CuGaSe_2$ and $CuInSe_2$. Although not in amplitude, the overall shape of the absorption coefficients, dielectric tensor components, refractive index, and reflectivity data computed using the LCAO-GGA method are similar

to spectroscopic ellipsometry data. After *ad hoc* scissor correction, the optical properties obtained from the FP-LAPW calculations are found to be in better agreement with the available spectroscopic ellipsometry data. The imaginary parts of the dielectric functions are discussed in terms of transitions between the valence and conduction bands. In addition, photovoltaic applications of both materials are interpreted in terms of their optical properties.

ACKNOWLEDGEMENTS

The authors are grateful to Prof. R. Dovesi and Prof. P. Blaha for providing the CRYSTAL03 and Wien2k computer codes, respectively. The authors are also thankful to the Council of Scientific and Industrial Research (CSIR), New Delhi (India) for financial support through Grant No. 03(1157)/10/EMR-II.

REFERENCES

1. J.E. Jaffe and A. Zunger, *Phys. Rev. B* 27, 5176 (1983).
2. J.E. Jaffe and A. Zunger, *Phys. Rev. B* 28, 5822 (1983).
3. J.E. Jaffe and A. Zunger, *Phys. Rev. B* 29, 1882 (1984).
4. N.N. Syrbu, M. Bogdanash, V.E. Tezlevan, and I.G. Stamov, *J. Phys. Condens. Matter* 9, 1217 (1997).
5. R.B.V. Chalapathy and K.T. Ramakrishna Reddy, *Adv. Mater. Sci. Technol.* 1, 1 (1998).
6. A.V. Mudryi, I.V. Bodnar, V.F. Gremenok, I.A. Victorov, A.I. Patuk, and I.A. Shakui, *Sol. Energy Mater. Sol. Cells* 53, 247 (1998).
7. S. Chichibu, T. Mizutani, K. Murakami, T. Shioda, T. Kurafuji, H. Nakanishi, S. Niki, P.J. Fons, and A. Yamada, *J. Appl. Phys.* 83, 3678 (1998).
8. T. Kawashima, S. Adachi, H. Miyake, and K. Sugiyama, *J. Appl. Phys.* 84, 5202 (1998).
9. R. Ahuja, S. Auluck, O. Eriksson, J.M. Wills, and B. Johansson, *Sol. Energy Mater. Sol. Cells* 53, 357 (1998).
10. J.A. Rodriguez, L. Quiroga, A. Camacho, and R. Baquero, *Phys. Rev. B* 59, 1555 (1999).
11. M.I. Alonso, K. Wakita, J. Pascual, M. Garriga, and N. Yamamoto, *Phys. Rev. B* 63, 075203 (2001).
12. S.N. Rashkeev and W.R.L. Lambrecht, *Phys. Rev. B* 63, 165212 (2001).
13. M. Belhadj, A. Tadjer, B. Abbar, Z. Bousahla, B. Bouhafs, and H. Aourag, *Phys. Stat. Sol. b* 241, 2516 (2004).
14. X. Jiang and W.R.L. Lambrecht, *Phys. Rev. B* 69, 035201 (2004).
15. N.I. Medvedeva, E.V. Shalaeva, M.V. Kuznetsov, and M.V. Yakushev, *Phys. Rev. B* 73, 035207 (2006).
16. S. Chen, X.G. Gong, and S.-H. Wei, *Phys. Rev. B* 75, 205209 (2007).
17. A.H. Reshak and S. Auluck, *PMC Phys. B* 1, 12 (2008).
18. S. Levchenko, N.N. Syrbu, V.E. Tezlevan, E. Arushanov, J.M. Merino, and M. Leon, *J. Phys. D Appl. Phys.* 41, 055403 (2008).
19. H. Zhao and C. Persson, *Thin Solid Films* (2011). doi: 10.1016/j.tsf.2010.12.217.
20. V.R. Saunders, R. Dovesi, C. Roetti, R. Orlando, C.M. Zicovich-Wilson, N.M. Harrison, K. Doll, B. Cevalleri, I.J. Bush, Ph. D'Arco, and M. Llunell, *CRYSTAL 2003 Users Manual* (Torino, Italy: University of Torino, 2003).
21. J.P. Perdew and A. Zunger, *Phys. Rev. B* 23, 5048 (1981).
22. J.P. Perdew, K. Burke, and M. Ernzerhof, *Phys. Rev. Lett.* 77, 3865 (1996).
23. A.D. Becke, *Phys. Rev. B* 38, 3098 (1988).
24. J.P. Perdew and Y. Wang, *Phys. Rev. B* 33, 8800 (1986).
25. C. Lee, W. Yang, and R.G. Parr, *Phys. Rev. B* 37, 785 (1988).
26. S.H. Vosko, L. Wilk, and M. Nusair, *Can. J. Phys.* 58, 1200 (1980).
27. P. Blaha, K. Schwarz, and J. Luitz, *Wien2K Code, An Augmented Plane Wave Plus Local Orbitals Program for Calculating Crystal Properties* (Vienna, Austria: Vienna University of Technology, 2001).
28. Z. Wu and R.E. Cohen, *Phys. Rev. B* 73, 235116 (2006).
29. C.A. Draxl and J.O. Sofo, *Comput. Phys. Commun.* 175, 1 (2006).
30. D. Ayma, J.P. Campillo, M. Rérat, and M. Causá, *J. Comput. Chem.* 18, 1253 (1997).
31. V. Sharma, S. Tiwari, and B.L. Ahuja, *Radiat. Phys. chem.* 79, 678 (2010).
32. V. Sharma and B.L. Ahuja, *Phys. Lett. A* 372, 5377 (2008).
33. D.R. Penn, *Phys. Rev.* 128, 2093 (1962).